tion and quantitative intensity measurements, the oxygen occupancy of individual lattice sites in defects can be measured. The basis for this is provided by the fact that the oxygen image signal depends linearly on occupancy and that the imaging parameters required for a quantitative evaluation can be determined by exploiting the dependence of the image signal of the neighboring cation columns on these parameters. The technique that we have described can be applied to more extensive studies on defects in oxides. In view of their importance in determining the electronic properties of these materials, quantitative oxygen concentration measurements offer potential, for example, in assessing the role of oxygen in grain-boundary Josephson junctions in oxide superconductors. Our technique is, however, not limited to oxides but can be applied to compounds such as nitrides and borides, in which deviations from stoichiometry with respect to low–nuclear charge atoms control the physical properties.

Second, our measurements provide quantitative evidence for a substantial reduction of the oxygen occupancy, i.e., the presence of oxygen vacancies in the $\Sigma3\{111\}$ twin boundaries in $BaTiO_3$. On average, 68% of the boundary oxygen sites are occupied and the others, about one site out of three, are left vacant. The error in the mean occupancy can be accounted for by an atomic-scale specimen surface roughness. Also, despite the low sensitivity of $BaTiO_3$ to electron radiation damage, a contribution of radiation-induced chemical disorder cannot be entirely ruled out.

From the results of an EELS study of the near-edge structure of the L_{23} ionization edge of Ti in the $\Sigma3\{111\}$ twin boundary, it was concluded that the Ti atoms adjacent to the boundary plane occur in an oxidation state lower than the +4 on the stoichiometric compound (*14*). This suggests that the boundary plane is oxygen deficient. In the $\Sigma3\{111\}$ twin boundary, the original TiO_6 octahedra change from corner- to face-sharing, forming a Ti_2O_9 group unit. This group is a genuine element of the $BaTiO_3$ system because it is also the basic structural element of the hexagonal high-temperature phase formed from the cubic phase at ~1460°C (*28*, *36*). In a study performed by x-ray scattering on $BaTiO_3$ in which tetravalent Ti^{4+} was replaced by trivalent Fe^{3+}, the hexagonal phase was obtained (*37*). In this hexagonal $Ba(Ti_{1-x}Fe_x)O_3$ phase, those sites [called O(1) sites] of the Ti_2O_9 group unit that correspond to the oxygen sites in our $\Sigma3\{111\}$ twin boundary plane are left partially vacant. When the iron content of the compound is varied, there is a maximum concentration of Fe^{3+} that can be accommodated. If we assume that the corresponding oxygen vacancies are all confined to the O(1) sites, this corresponds to an occupancy in which one oxygen atom in three is missing. Because the structure of the bulk hexagonal phase and the structure of the $\Sigma3\{111\}$ twin boundary are both based on the Ti_2O_9 group unit, our measured oxygen occupancy of 68% for the oxygen boundary sites is in excellent agreement with the results obtained in the bulk $Ba(Ti_{1-x}Fe_x)O_3$ phase. Thus, the incorporation of oxygen vacancies reduces the grain boundary energy and allows the system to react to oxygen-deficient conditions, e.g., during thin-film deposition, by the formation of a nanotwin lamella structure.

To date no theoretical calculations are available for an oxygen-deficient structure of the $\Sigma3\{111\}$ twin boundary in $BaTiO_3$. However, for $SrTiO_3$, it has recently been shown by first-principles calculations that incorporation of oxygen vacancies in the grain boundary plane is expected to reduce the total energy of the boundary even though the Ti valence deviates from the value in the stoichiometric compound (*9*, *38*). Our measurements now open up the possibility of constructing realistic models for advanced electronic-structure calculations in these materials.

References and Notes

1. N. Setter, R. Waser, *Acta Mater.* **48**, 151 (2000).
2. H.-I. Yoo, C.-R. Song, D.-K. Lee, *J. Electroceram.* **8**, 5 (2002).
3. C. P. Poole, H. A. Farach, R. J. Creswick, *Superconductivity* (Academic Press, San Diego, CA, 1995).
4. Y. Tokura, *Colossal Magnetoresistive Oxides* (Gordon & Breach, London, 2000).
5. R. Waser, *Integr. Ferroelect.* **15**, 39 (1997).
6. A. K. Tagantsev, I. Stolichnov, E. L. Colla, N. Setter, *J. Appl. Phys.* **90**, 1387 (2001).
7. R. Waser, *Solid State Ionics* **75**, 89 (1995).
8. R. F. Klie, Y. Ito, S. Stemmer, D. N. Browning, *Ultramicroscopy* **86**, 289 (2001).
9. M. Kim *et al.*, *Phys. Rev. Lett.* **86**, 4056 (2001).
10. A. Ourmazd, J. C. H. Spence, *Nature* **329**, 425 (1987).
11. N. P. Huxford, D. J. Eaglesham, C. J. Humphreys, *Nature* **329**, 812 (1987).
12. G. Van Tendeloo, T. Krekels, in *Characterization of High T_C Materials & Devices by Electron Microscopy*, N. D. Browning, S. J. Pennycook, Eds. (Cambridge Univ. Press, Cambridge, 2000), pp. 161–191.
13. Z. Zhang, W. Sigle, F. Phillipp, M. Rühle, *Science* **302**, 846 (2003).
14. A. Recnik *et al.*, *Philos. Mag. B* **70**, 1021 (1994).
15. Z. Zhang, W. Siegle, M. Rühle, *Phys. Rev. B* **66**, 94108 (2002).
16. C. L. Jia, M. Lentzen, K. Urban, *Science* **299**, 870 (2003).
17. C. L. Jia, M. Lentzen, K. Urban, *Microsc. Microanal.*, in press.
18. C. L. Jia *et al.*, *Philos. Mag. A* **77**, 923 (1998).
19. T. Suzuki, Y. Nishi, M. J. Fujimoto, *J. Am. Ceram. Soc.* **83**, 3185 (2000).
20. K. P. Fahey, B. M. Clemens, L. A. Wills, *Appl. Phys. Lett.* **67**, 2480 (1995).
21. M. Haider *et al.*, *Nature* **392**, 768 (1998).
22. All intensity data are taken from the original unfiltered images.
23. M. Lentzen *et al.*, *Ultramicroscopy* **92**, 233 (2002).
24. H. Lichte, *Ultramicroscopy* **38**, 13 (1991).
25. All calculations and numerical image simulations were carried out with the *MacTempas* software package (M. A. O'Keefe, R. Kilaas; National Center for Electron Microscopy, Lawrence Berkeley National Laboratory, Univ. of California).
26. J. M. Cowley, A. F. Moodie, *Acta Crystallogr.* **10**, 609 (1957).
27. M. A. O'Keefe, R. Kilaas, *Scanning Microsc. Suppl.* **2**, 225 (1988).
28. C. L. Jia, A. Thust, *Phys. Rev. Lett.* **82**, 5052 (1999).
29. A. Ourmazd, F. H. Baumann, M. Bode, Y. Kim, *Ultramicroscopy* **34**, 237 (1990).
30. D. Stenkamp, W. Jäger, *Ultramicroscopy* **50**, 321 (1993).
31. C. Kisielowski *et al.*, *Ultramicroscopy* **58**, 131 (1995).
32. The computer code "Digital Micrograph" (GATAN) is used for this purpose.
33. M. J. Hÿtch, W. M. Stobbs, *Ultramicroscopy* **53**, 63 (1994).
34. A. Thust, K. Urban, *Ultramicroscopy* **45**, 23 (1992).
35. W. E. King, G. H. Campbell, *Ultramicroscopy* **56**, 46 (1994).
36. R. D. Burbank, H. T. Evans, *Acta Crystallogr.* **1**, 330 (1948).
37. I. E. Grey *et al.*, *J. Solid State Chem.* **135**, 312 (1998).
38. R. Astala, P. D. Bristowe, *J. Phys. Condens. Matter* **14**, 6455 (2002).

39. We thank A. Thust, M. Lentzen, K. Tillmann, and L. Houben for fruitful discussions and comments on the manuscript.

13 November 2003; accepted 13 February 2004

Oxygen Isotope Constraints on the Sulfur Cycle over the Past 10 Million Years

Alexandra V. Turchyn* and Daniel P. Schrag

Oxygen isotopes in marine sulfate ($\delta^{18}O_{SO4}$) measured in marine barite show variability over the past 10 million years, including a 5 per mil decrease during the Plio-Pleistocene, with near-constant values during the Miocene that are slightly enriched over the modern ocean. A numerical model suggests that sea level fluctuations during Plio-Pleistocene glacial cycles affected the sulfur cycle by reducing the area of continental shelves and increasing the oxidative weathering of pyrite. The data also require that sulfate concentrations were 10 to 20% lower in the late Miocene than today.

Sulfate plays an important role in the modern ocean, serving as the primary oxidant for much of the organic matter and nearly all of the methane produced in ocean sediments (*1*, *2*). The biogeochemical cycle of marine sulfate has been assumed to be relatively stable, with a long residence time of ~10^7 years (*3*–*6*). Studies of marine sulfate, focusing largely on variations of sulfur isotopes in sedimentary pyrite (*7*, *8*), have concluded that sulfate concentrations were low in the Archean, increased in the Proterozoic to modern

values (*7*, *9*), and have remained high through the Phanerozoic (*9*, *10*).

The amount of sulfate in the ocean is controlled by three major processes: input from rivers, sulfate reduction and sulfide reoxidation on continental shelves and slopes, and burial of anhydrite and pyrite in the ocean crust. Sulfate reduction and sulfide reoxidation on continental shelves and slopes dominate the sulfate budget in the modern ocean. Reduction rates decrease from more than 10 to ~0.002 mol/m^2/year from the continental shelf to the slope (*1*, *2*, *11*–*15*), resulting in a global average reduction rate of 8×10^{12} to 11×10^{12} mol/year, about three times the river flux (2×10^{12} to 3.5×10^{12} mol/year) (*5*, *16*). Most of the sulfide produced by sulfate reduction is subsequently reoxidized (75 to 90%) (*11*–*13*), so this processing of sulfate in organic sediments is neglected when the residence time of sulfate in seawater is calculated. However, the reduction and reoxidation affects the oxygen isotopic composition of sulfate, so the effective residence time for oxygen isotopes in sulfate is 1 to 1.5 million years (My), much shorter than when one considers riverine input alone. Sulfate burial in the ocean crust as anhydrite or pyrite has been estimated at 0.5×10^{12} to 4.1×10^{12} mol/year (*5*, *17*). Smaller fluxes in the sulfate cycle include sulfate-associated carbonate precipitation (0.15×10^{12} mol/year) (*18*), serpentization of the ocean crust (0.01×10^{12} to 0.2×10^{12} mol/year) (*19*), and sulfide venting from ocean hydrothermal systems (0.2×10^{12} to 0.5×10^{12} mol/year) (*20*).

Oxygen is continually incorporated into the sulfate cycle through sulfide oxidation and released through sulfate reduction. The oxygen isotopic composition of sulfate ($\delta^{18}O_{SO4}$) in the modern ocean is 9.3 per mil (‰) (*21*, *22*), which is not in equilibrium with the ocean because isotopic exchange between sulfate and water is extremely slow at low temperatures and ocean pH (the time scale for exchange is ~10 My) (*21*, *23*). Different sources of sulfate to the ocean appear to have a range of oxygen isotopic compositions, indicating that $\delta^{18}O_{SO4}$ may be a useful tracer for the biogeochemical sulfate cycle. Natural riverine $\delta^{18}O_{SO4}$ is –2 to +7‰ (*24*), which is a mixture of weathered evaporite deposits that are 11 to 13‰ (*3*) and oxidative pyrite weathering that is –4 to +2‰ (*25*). Sulfate reduction preferentially selects sulfate with lighter oxygen isotopes, but sulfate-enzyme coupling also allows isotopic exchange between sulfate and water during reduction, which leaves the residual sulfate pool initially 8 to 10‰ enriched over seawater and up to 25‰ enriched in sulfate-limited environments (*26*). Sulfide reoxidation on continental shelves, dominated in the modern ocean by bacterial disproportionation, produces sulfate that is enriched by 8 to 17‰ over the $\delta^{18}O$ of seawater, depending on the metal oxide present (*27*, *28*). Finally, direct sulfide oxidation, which occurs in hydrothermal environments and some shallow sediment environments, produces sulfate with about the same $\delta^{18}O$ as the seawater in which it was oxidized (*24*).

We studied temporal changes in the marine sulfate cycle through analysis of the $\delta^{18}O$ of marine barite ($BaSO_4$). Marine barite has been shown to be a reliable recorder of Cenozoic seawater strontium and sulfur isotopic composition (*29*, *30*). Barite offers advantages over other sulfate minerals for studying paleo-$\delta^{18}O_{SO4}$, because of its resistance to diagenesis in pelagic sediments and the uninterrupted record not afforded by sulfate evaporite deposits (*29*). Barite was extracted from sediments with a method designed to reduce oxygen isotope exchange between sulfate and water (*31*). Pelagic sediments were selected from Deep-Sea Drilling Program (DSDP) sites in the tropical Pacific Ocean, because of previous success in the extraction of usable amounts of trace barite from these sites (*29*, *30*) and because porewater sulfate concentrations remain high throughout the sediment column, precluding barite diagenesis.

The $\delta^{18}O_{SO4}$ record in marine barite is shown in Fig. 1A. The $\delta^{18}O_{SO4}$ remains fairly constant around 9.5‰ (standard deviation 0.6‰) from 10 My ago (Ma) until 6 Ma. From 6 Ma to 3.5 Ma, it rises monotonically to 12.5‰. This increase is followed by a decline of 5‰, starting ~3 Ma, to a consistent modern value of 7.9‰. The decline coincides with a 1.5‰ increase in the $\delta^{18}O$ of benthic foraminifera (Fig. 1B) (*32*). The isotopic offset between modern marine barite and sulfate (1.4‰) is most likely a kinetic isotope effect associated with rapid barite precipitation in the modern ocean. This trend is reproduced at five sites, each with different sedimentation histories.

We used a numerical model (*33*) (supporting online material) to explore what the $\delta^{18}O_{SO4}$ record implies about the sulfate biogeochemical cycle. Coupled conservation equations in the model allowed us to simultaneously monitor changes in the amount of sulfate in the ocean and the $\delta^{18}O_{SO4}$. The main parameters in the model are river input, sulfate reduction rates, sulfide reoxidation rates (as a percentage of the reduction rate), and a burial term associated with anhydrite and pyrite burial in hydrothermal systems. Sulfate reduction rates were modeled as a function of both shelf area and marine sulfate concentrations, where the initial input was calculated from a compilation of literature values (*1*, *2*, *11*–*15*).

The persistence of slightly enriched $\delta^{18}O_{SO4}$ in the late Miocene from 10 to 6 Ma is consistent with a steady-state sulfate concentration of 22 to 25 mM and with a smaller fraction of sulfide reoxidized on continental shelves than during the Plio-Pleistocene (required to produce the large drop in $\delta^{18}O_{SO4}$ discussed below). One possibility for a smaller fraction of sulfide reoxidation is higher iron availability, enhancing the formation of pyrite. Our model also suggests that sulfide reoxidation during the Miocene was dominated by reactions that produced sulfate with $\delta^{18}O$ of 10 to 14‰, which is consistent with disproportionation reactions in the presence of iron (*27*). The monotonic increase in $\delta^{18}O_{SO4}$ from 6 to 3 Ma can be explained by a shift to other reoxidation pathways that produce isotopically enriched sulfate. We modeled this change as a shift from

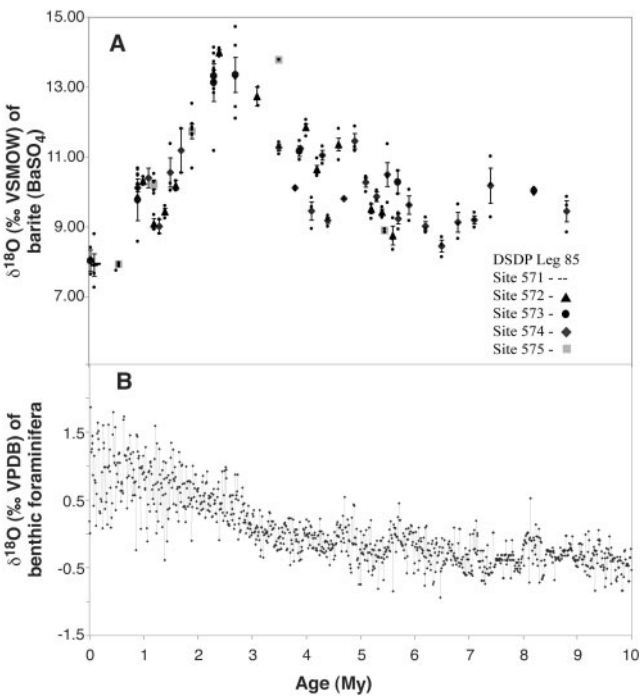

Fig. 1. (**A**) The $\delta^{18}O_{SO4}$ data for the past 10 My, measured in marine barite. Error bars are standard error, calculated from replicate measurements of each sample (small dots). (**B**) The $\delta^{18}O$ benthic foraminifera from Zachos *et al*. (*30*). The increase in $\delta^{18}O$ at 3 Ma coincides with the beginning of the decrease in the $\delta^{18}O_{SO4}$. VPDB, Vienna Pee Dee Belemnite.

Department of Earth and Planetary Sciences, Harvard University, Cambridge, MA 02138 USA.

*To whom correspondence should be addressed. E-mail: avan@fas.harvard.edu

disproportionation reactions in the presence of predominantly iron (10 to 14‰) to disproportionation in the presence of manganese (16 to 18‰) (*28*). This shift would also be associated with a small increase in the reoxidation percentage, as less iron would mean less sulfide scavenged as pyrite. This is why a small increase in sulfate concentrations is observed in our model between 6 and 3 Ma.

Modeling the large drop in $\delta^{18}O_{SO4}$ over the past 3 My requires both a shift from isotopically heavy sources, such as sulfide reoxidation dominated by sulfur disproportionation, to isotopically lighter sources, such as oxidative pyrite weathering (which produces sulfate with a $\delta^{18}O_{SO4}$ of −4 to +2‰), and an increase in the fluxes associated with the lighter sources. Because of the need for an increase in the lighter isotope fluxes, the 5‰ decline in $\delta^{18}O_{SO4}$ is difficult to explain unless sulfate concentrations increased over the Plio-Pleistocene while the $\delta^{18}O_{SO4}$ decreased. This implies that sulfate concentrations were 10 to 20% lower in the Miocene. A likely explanation for this change is that sea level fluctuations during the Plio-Pleistocene glacial cycles changed the area of continental shelves, disrupting the processing of sulfate in organic-rich sediments. Oxidative pyrite weathering on exposed shelves during glacial episodes provides sulfate to the ocean that is an additional isotopically light source. During glacial maxima, this additional pyrite weathering flux is 5×10^{12} mol/year, or nearly twice the current river flux. Although sulfate reduction and reoxidation rates decrease substantially when shelf area is reduced, the sulfide reoxidation rate along with the additional pyrite weathering rate contributes to a net increase in flux of sulfate to the ocean, driving sulfate concentrations higher.

Our model suggests that the addition of pyrite weathering on exposed continental shelves alone would reduce $\delta^{18}O_{SO4}$ by 1.5‰ over the past 3 My (Fig. 2). In order for the full 5‰ decrease seen in these 3 My to occur without a change in the isotope fractionation associated with barite precipitation, two additional parameters associated with sulfur cycling on continental shelves and slopes must change. First, the amount of sulfide reoxidized on continental shelves must increase from a Miocene value of 60 to 70% to a Plio-Pleistocene value of 75 to 85%, implying that reduced sulfate has been more readily reoxidized over the past 3 My, which would also contribute to increasing sulfate concentrations. A possible explanation for this is that higher dissolved oxygen levels in the glacial ocean, because of colder deep-ocean temperatures (*34*) as well as possibly higher amounts of O_2 in the atmosphere (*35*), may yield faster reoxidation at the sediment/water interface. The second change required to model the full isotopic decline is that sulfide reoxidation pathways cannot be dominated by disproportionation reactions. The full 5‰ decline is only realized when the fractionation associated with reoxidation decreases to ~2‰ at glacial maxima when sea levels are lowest (Fig. 2). This suggests a fundamental change in redox chemistry during the Plio-Pleistocene: Lower sea levels, with colder temperatures and higher oxygen availability, may lead to substantial changes in the pathways by which sulfur cycles in the sediments, perhaps causing sulfide reoxidation to be dominated by direct oxidation pathways, which produce sulfate with a similar isotopic composition to seawater.

This study highlights the processing of sulfur on continental shelves and slopes as the driver of rapid changes in marine $\delta^{18}O_{SO4}$. Substantial changes in river fluxes or the isotopic composition of river input cannot affect $\delta^{18}O_{SO4}$ over short time scales. This may also explain why the $\delta^{34}S$ in marine barite declines by only 0.8‰ over the time period when the $\delta^{18}O$ declines by 5‰. The reduction and subsequent reoxidation of sulfur in organic-rich sediments resets the $\delta^{18}O$, but because 90% is reoxidized, the sulfur isotopes of the returning sulfate are largely conserved. We suggest that the 0.8‰ decline in $\delta^{34}S$ over the Plio-Pleistocene may reflect the input of isotopically light sources from the weathering of pyrite on exposed continental shelves or the decreased burial of pyrite due to lower shelf area.

Our data demonstrate the dynamic nature of the sulfur cycle and suggest that major changes in the sulfur cycle are possible at other points in Earth's history when disruptions to processes on continental shelves and slopes occurred. Because sulfate serves as the primary oxidant for many biochemicals, including its critical role in anaerobic methane oxidation, the redox capacity of the ocean may be quite variable through the Phanerozoic.

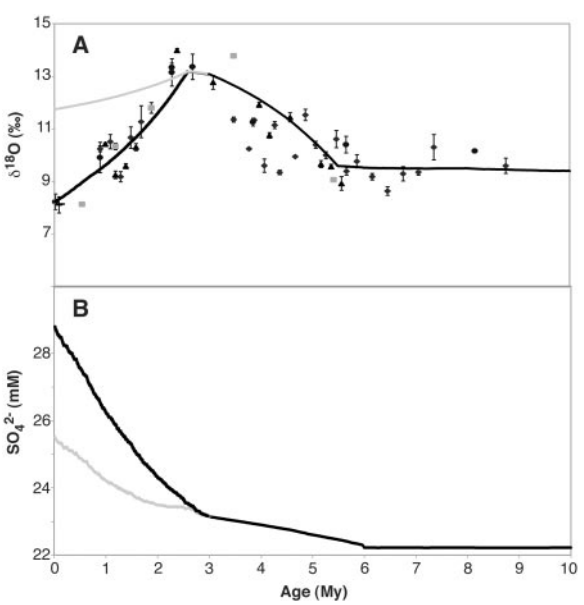

Fig. 2. (**A**) Model results for the $\delta^{18}O_{SO4}$ over the past 10 My compared with observed $\delta^{18}O_{SO4}$ data. The gray curve represents the modeled $\delta^{18}O_{SO4}$ if the decrease in $\delta^{18}O_{SO4}$ is due only to increased pyrite weathering on exposed continental shelves during glacial cycles. The black curve represents the modeled $\delta^{18}O_{SO4}$ when changes in sulfur cycling are induced between the Miocene and Plio-Pleistocene in addition to the pyrite weathering, including an increased percentage of sulfide reoxidized and decreased reoxidated fractionation. Data symbols are the same as in Fig. 1. (**B**) Model results for sulfate concentration for the two model scenarios. The small increase in sulfate concentration between 6 and 3 Ma is due to a small increase in reoxidation percentage.

References and Notes

1. C. Niewöhner, C. Hensen, S. Kasten, M. Zabel, H. D. Schulz, *Geochim. Cosmochim. Acta* **62**, 455 (1998).
2. S. Kasten, B. B. Jørgensen, in *Marine Geochemistry*, H. D. Schulz, M. Zabel, Eds. (Springer-Verlag, Berlin, 2000), pp. 263–275.
3. G. E. Claypool, W. T. Holser, I. R. Kaplan, H. Sakai, I. Zak, *Chem. Geol.* **28**, 199 (1980).
4. W. T. Holser, I. R. Kaplan, H. Sakai, I. Zak, *Chem. Geol.* **25**, 1 (1979).
5. J. C. G. Walker, *Mar. Geol.* **70**, 159 (1986).
6. S. T. Petsch, R. A. Berner, *Am. J. Sci.* **298**, 246 (1998).
7. D. E. Canfield, A. Teske, *Nature* **382**, 697 (1996).
8. D. E. Canfield, K. S. Habicht, B. Thamdrup, *Science* **288**, 658 (2000).
9. K. S. Habicht, M. Gade, B. Thamdrup, P. Berg, D. E. Canfield, *Science* **298**, 2372 (2002).
10. D. E. Canfield, R. Raiswell, *Am. J. Sci.* **299**, 697 (1999).
11. B. B. Jørgensen, *Nature* **296**, 643 (1982).
12. D. E. Canfield, *Am. J. Sci.* **291**, 177 (1991).
13. S. Lin, J. W. Morse, *Am. J. Sci.* **291**, 55 (1991).
14. S. D'Hondt, S. Rutherford, A. J. Spivack, *Science* **295**, 2067 (2002).
15. B. Thamdrup, H. Fossing, B. B. Jørgensen, *Geochim. Cosmochim. Acta* **58**, 5115 (1994).
16. M. Meybeck, *Rev. Geol. Dynam. Geograph. Phys.* **21**, 215 (1979).
17. R. E. McDuff, J. M. Edmond, *Earth Planet. Sci. Lett.* **57**, 117 (1982).
18. H. Strauss, *Chem. Geol.* **161**, 89 (1999).
19. J. C. Alt, W. C. Shanks, *Geochim. Cosmochim. Acta* **67**, 641 (2003).
20. K. L. Von Damm, in *Seafloor Hydrothermal Systems: Physical, Chemical, Biological, and Geological Interactions*, S. E. Humphries, R. A. Zierenberg, L. S. Mullineaux, R. W. Thomson, Eds. (American Geophysical Union, Washington DC, 1995), pp. 173–204.
21. R. M. Lloyd, *J. Geophys. Res.* **73**, 6099 (1967).
22. A. Longinelli, H. Craig, *Science* **156**, 56 (1968).
23. M. Kukasabe, B. W. Robinson, *Geochim. Cosmochim. Acta* **41**, 1033 (1968).
24. D. R. Van Stempvoort, H. R. Krouse, in *Environmental Geochemistry of Sulfide Oxidation*, C. N. Alpers, D. W. Blowes, Eds. (American Chemical Society, Washington, DC, 1994), pp. 446–480.
25. H. R. Krouse, B. Mayer, in *Environmental Tracers in Subsurface Hydrology*, P. G. Cook, A. L. Herczeg, Eds. (Kluwer, Lowell, MA, 2000), pp. 195–231.
26. P. Fritz, G. M. Basharmal, R. J. Drimmie, J. Isben, R. M. Qureshi, *Chem. Geol.* **79**, 99 (1989).
27. M. E. Böttcher, B. Thamdrup, *Geochim. Cosmochim. Acta* **65**, 1573 (2001).

28. M. E. Böttcher, B. Thamdrup, T. W. Vennemann, *Geochim. Cosmochim. Acta* **65**, 1601 (2001).
29. A. Paytan, M. Kastner, E. E. Martin, J. D. MacDougall, T. Herbert, *Nature* **366**, 445 (1993).
30. A. Paytan, M. Kastner, D. Campbell, M. H. Thiemens, *Science* **282**, 1459 (1998).
31. Sediment was digested in 1 M acetic acid (pH ≈ 3) to dissolve the carbonate. The remaining sediment was repeatedly rinsed with distilled water, dried, manually ground to powder, and sieved to 200 μm. We suspended the powder in a 2.85 g/cc lithium polytungstate solution to separate barite from clays. All higher density material was extracted and rinsed with distilled water. Residual organic matter was oxidized in sodium hypochlorite warmed to 50°C and acidified with HCl. We washed the residue in 0.02 M hydroxylamine hydrochloride in 10 volume percent acetic acid to clear the barite of transition metal oxyhydroxides. All samples were measured for purity on an x-ray diffractometer (XRD), and samples that had nonbarite XRD lines were further purified or reextracted. All samples run for oxygen isotope analysis were assumed to be 97% pure. Oxygen isotopes were measured through pyrolysis in a Thermal Combustion Element Analyzer coupled to a Delta Plus mass spectrometer, then corrected to Vienna Standard Mean Ocean Water (VSMOW). NB5127 (NBS) barite was measured at 9.73 ± 0.42‰, indicating the measurement technique was sufficiently accurate and precise. Two separate barite standards were run with all samples for internal verification and drift correction. All samples were corrected to an NBS barite value of 9.3‰.
32. J. Zachos, M. Pagani, L. Sloan, E. Thomas, K. Billups, *Science* **292**, 686 (2001).
33. We modeled the sulfate cycle using the following conservation equation for sulfate: $\partial(M_{SO4})/dt = J_{rivers} - J_{reduc} + f \times J_{reduc} - J_{burial}$, where M_{SO4} is the amount of sulfate, t is time, J_{rivers} is the river sulfate flux, J_{reduc} is the sulfate reduction rate, f is the fraction of sulfide reoxidized, and J_{burial} is anhydrite and pyrite burial. For sulfate oxygen isotopes, we used $\partial(\delta^{18}O_{SO4}M_{SO4})/dt = J_{rivers}(\delta^{18}O_{SO4\text{-}riv}) + f \times J_{reduc}[(\delta^{18}O_{SW} + X) - \delta^{18}O_{SO4}] - J_{reduc}[\delta^{18}O_{SO4} - (\delta^{18}O_{SW} + Y)] - J_{burial}(\delta^{18}O_{SO4})$, where $\delta^{18}O_{SO4\text{-}riv}$ is the river sulfate $\delta^{18}O$, X is the ‰ fractionation associated with sulfide reoxidation, and Y is the ‰ fractionation associated with residual sulfate during sulfate reduction. The value used for J_{rivers} was 3×10^{12} mol/year, $\delta^{18}O_{SO4\text{-}riv}$ is 4‰, $\delta^{18}O_{SW}$ varies as per (*30*), X is 15‰ in the modern ocean, and Y is 10‰ in the modern ocean (*26*). J_{reduc} is a function of both shelf area and M_{SO4}; we estimated the initial value by modeling measured rates as an exponential function of water depth, yielding a global rate of 8×10^{12} to 11.0×10^{12} mol/year. f is 83% in the modern ocean (but might be closer to 65% in the Miocene). J_{burial} is a function of M_{SO4} with an initial value of 1×10^{12} mol/year. We modeled the evolution of sulfate and $\delta^{18}O_{SO4}$ over the past 10 My using finite difference with a time step of 10,000 years. Sea levels were calculated with the $\delta^{18}O$ in benthic foraminifera curve from (*30*). Sea level change between today and the last glacial maximum was assumed to be 130 m.
34. D. P. Schrag, G. Hampt, D. W. Murray, *Science* **272**, 1930 (1996).
35. L. A. Derry, C. France-Lanord, *Paleoceanography* **11**, 267 (1996).
36. We thank L. Derry and one anonymous reviewer for suggestions that greatly improved this manuscript. Supported by a Department of Defense American Society for Engineering Education Graduate Fellowship (A.V.T.) and NSF grant no. OCE-0096909 (D.P.S).

Supporting Online Material
www.sciencemag.org/cgi/content/full/303/5666/2004/DC1
SOM Text
Fig. S1
Table S1
References and Notes

7 October 2003; accepted 26 January 2004

Actin Polymerization–Driven Molecular Movement of mDia1 in Living Cells

Chiharu Higashida,[1] Takushi Miyoshi,[1] Akiko Fujita,[1] Fabian Oceguera-Yanez,[1] James Monypenny,[1] Yoshikazu Andou,[1] Shuh Narumiya,[1] Naoki Watanabe[1,2]*

mDia1, a Rho effector, belongs to the Formin family of proteins, which shares the conserved tandem FH1-FH2 unit structure. Formins including mDia1 accelerate actin nucleation while interacting with actin filament fast-growing ends. Here our single-molecule imaging revealed fast directional movement of mDia1 FH1-FH2 for tens of microns in living cells. The movement of mDia1 FH1-FH2 was blocked by actin-perturbing drugs, and the speed of mDia1 FH1-FH2 movement appeared to correlate with actin elongation rates. In vitro, mDia1 FH1-FH2 associated persistently with the growing actin barbed end. mDia1 probably moves processively along the growing end of actin filaments in cells, and Formins may be a molecular motility machinery that is independent from motor proteins.

Formin homology proteins (Formins) play essential roles in the regulation of specific actin-based structures (*1*, *2*), e.g., the contractile ring in cytokinesis (*3*, *4*); actin cables in budding yeasts (*5*–*7*); and actin fibers in animal cells (*8*). The structure of Formins is conserved in most of the C-terminal half including the FH1 and FH2 domains. The FH1 domain consists of poly-proline repeats that bind to profilin, and it is followed by conserved sequences of ~400 amino acids including the FH2 domain. This structural feature unique to Formins, called the FH1-FH2 unit (FH1-FH2) (*8*), implies a certain evolutionarily conserved function of FH1-FH2.

Yeast Formins (*9*–*12*) and mDia1 (*13*) have an actin nucleation-promoting activity in their FH1-FH2 or FH2 fragments. Nucleated actin filaments elongate at the fast-growing, barbed end. Formins have thus emerged as potential cellular actin nucleators. However, in marked contrast to the Arp2/3 complex, another actin nucleator, Formins bind the barbed end of actin filaments. Two models for how Formins allow barbed end elongation while binding the same site have been proposed. One is the profilin-gated mechanism for the barbed end capping by *Schizosaccharomyces pombe* Cdc12p (*12*). Alternatively, Bni1p and mDia1 function as "a leaky cap," and it has been postulated that Bni1p might "walk" along the barbed end of an elongating filament (*11*, *14*).

To explore the biochemical properties of Formins in living cells, we took an approach similar to single-molecule actin speckle analysis (*15*). We expressed mDia1 mutants fused to an enhanced green fluorescent protein (EGFP) (Fig. 1A) in XTC fibroblasts and carried out live-cell imaging of mDia1 expressed at a low level (*16*). mDia1△N3, an FH1-FH2 mutant, induced the formation of massive thin actin fibers, reminiscent of Rho-induced actin stress fibers (Fig. 1B) (*8*). Speckle microscopy revealed fast, directional molecular movement of EGFP-mDia1△N3 (Fig. 1C, Movie S1). Fluorescence intensity of moving signals was comparable to that of single-molecule EGFP-actin (*15*), which indicated that they consisted of single EGFP or a few EGFP molecules coupled to multimeric mDia1 (*13*). mDia1△N3 movement persisted along a long path that often spanned the radius of the cell (from the center to the edge). mDia1△N3 speckles could be tracked along a line or a wide arc, which suggests an association with certain cytoskeletal filaments. At the cell periphery, the majority of mDia1△N3 speckles moved outward along filopodium-like protrusions, accumulating in the tip region (Fig. 1B, inset; Movie S1). We also observed movement of mDia1F2 speckles. mDia1F2 is a mutant that is defective in promoting actin fiber formation (Fig. 1B) (*8*), and it weakly activates serum response factor (*17*). mDia1F2 speckles displayed slower rates of movement and traveled over shorter distances (Fig. 1D, Movie S2). The average speed of mDia1△N3 and mDia1F2 movement was 2.0 μm/s and 0.13 μm/s, respectively (Fig. 1E). The speed of mDia1△N3 movement is two orders of magnitude faster than the flow rate of the actin network (typically ~0.025 μm/s in lamellipodia of XTC cells) (*15*).

Unlike mDia1△N3 and mDia1F2, an EGFP-fusion of full-length mDia1, mDia1Full hardly exhibited any fast directional movement (Fig. 1F, left; Movie S3, top). We then tested whether administration of Rho affects the mobility of mDia1Full, as Rho binding to the mDia1 N terminus has been postulated to disrupt the autoinhibitory intramolecular interaction of mDia1, by exposing FH1-FH2 and thus permitting its

[1]Department of Pharmacology, Kyoto University Faculty of Medicine, Yoshida Konoe-cho, Sakyo-ku, Kyoto, Japan. [2]PRESTO, Japan Science and Technology Agency, 4-1-8 Honcho Kawaguchi, Saitama, Japan.

*To whom correspondence should be addressed. E-mail: naoki-w@mfour.med.kyoto-u.ac.jp